Highly Charged $^{229}Th^{6+}$ Ions as the Candidate Platform for Nuclear Clock

Shi-Cheng Yu[1,3†], Xia Hua[2†], Xin Tong[2,4*], Cheng-Bin Li[1*], and Lei She[1*]

[1]*Key Laboratory of Atom Frequency Standards, Innovation Academy for Precision Measurement Science and Technology, Chinese Academy of Sciences, Wuhan 430071, China*
[2]*State Key Laboratory of Magnetic Resonance and Atomic and Molecular Physics, Innovation Academy for Precision Measurement Science and Technology, Chinese Academy of Sciences, Wuhan 430071, China*
[3]*University of Chinese Academy of Sciences, Beijing 100049, China*
[4]*Wuhan Institute of Quantum Technology, Wuhan 430206, China*

(Received 31 August 2025; accepted manuscript online 15 October 2025)

The ^{229}Th nuclear optical clocks, operating via the 8.4 eV nuclear transition, hold great promise for attaining unprecedented accuracy in frequency standards and fundamental physics tests. In this study, we propose an approach that utilizes highly charged $^{229}Th^{6+}$ ions as the platform for nuclear clock, which exhibits simple electronic energy structures and enhanced nucleus–electron coupling compared to low-charge Th ions. The $^3P_2 \leftrightarrow {}^3P_0$ ionic clock transition in $^{229}Th^{6+}$ ions has the potential to serve as a probe for nuclear structure. Moreover, we predict the existence of two excited electronic states near and slightly above the nuclear clock state, which can serve as the intermediate states in the optical repumping process. We estimate the Rabi frequencies of the electronic bridge transitions from the nuclear clock state to these intermediate states and further analyze the population dynamics of the optical repumping process, which can be completed on the millisecond timescale. Our results demonstrate the advantages of using $^{229}Th^{6+}$ ions as the promising platform for nuclear clock.

DOI: 10.1088/0256-307X/42/12/120302 CSTR: 32039.14.0256-307X.42.12.120302

Optical clocks are outstanding instruments that play pivotal roles in global navigation systems, synchronizing communication networks, and advancing new physics research.[1,2] Among the candidates for next-generation optical clocks, the ^{229}Th nucleus stands out as a particularly promising option due to its unique properties, including a nuclear transition energy of 8.4 eV, an extremely narrow linewidth, remarkable insensitivity to external fields, and enhanced sensitivity to variations in the fine-structure constant.[3–10]

Nuclear clocks based on ions exhibit excellent potential in terms of accuracy.[11,12] Grounded in high-precision relativistic atomic structure calculations and a well-established theoretical framework for nuclear–electronic-external field interactions, the nuclear clock based on single Th^{3+} ion is predicted to achieve an accuracy of approximately 10^{-19} in fractional uncertainty.[11,12] Besides Th^{3+} ion, low-charge ions such as Th^+ and Th^{2+} have also been studied, with their electronic transitions serving as probes for nuclear structure information.[13–17] Moreover, Th^+, Th^{2+}, and Th^{4+} ions are also proposed as the viable options for nuclear clock.[18–21]

While previous research has predominantly focused on low-charge Th ions, only a limited number of studies have explored highly charged Th ions.[22–24] Additionally, there is a lack of research focusing on the optical repumping process in ion-based nuclear clocks. In this work, we propose highly charged ions, Th^{6+}, as the promising platform for a nuclear clock. The high ionization degree of Th^{6+} results in a simpler electronic structure and stronger nuclear–electronic interactions, which enables high-precision probing of nuclear structure information via electronic clock transitions, thereby enhancing our understanding of the ^{229}Th nucleus. We further propose that using the electronic bridge (EB) transition to the intermediate states can achieve optical repumping from the clock state to the ground state of nuclear clock on the millisecond timescale, significantly reducing the dead time waiting for spontaneous radiation from the nuclear clock state.

Figure 1 illustrates the four low-lying states of Th^{6+} with the electronic configuration $[Hg]6p^4$. Their energy ordering is analogous to that of Ba^{4+}, which confers similar advantages on the ionic clock transition: a clock state lifetime well-matched to the interrogation times of state-of-the-art cavity-stabilized lasers, low clock state multiplicity, and the potential for reduced systematic uncertainties.[25] A relatively low ionization energy of approximately 80 eV makes Th^{6+} easier to produce compared to other highly charged ions.[26] Moreover, $^{229}Th^{6+}$ can potentially be obtained as an alpha-decay product of ^{233}U.[13]

To study the clock performance in detail, we perform the configuration interaction (CI) with many-body perturbation theory calculations using the AMBiT package.[27] The CI space is formed by single and double excitations to orbitals 23spdfgh from reference configuration $6s^26p^4$. We label the ionic clock transition and nuclear clock

†These authors contributed equally to this work.
*Corresponding authors. Email: tongxin@wipm.ac.cn; cbli@apm.ac.cn; shelei@apm.ac.cn
© 2025 Chinese Physical Society and IOP Publishing Ltd. All rights, including for text and data mining, AI training, and similar technologies, are reserved.

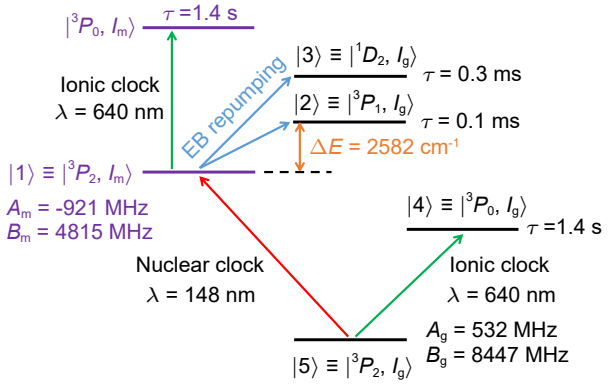

Fig. 1. Diagram of low-lying states and clock transitions. The purple energy level represents the nuclear isomer state I_m. The radiative lifetimes of the electronic states are indicated. The nuclear isomer state has a radiative lifetime of 1740 s.[8] The hyperfine structure constants A and B for the ground state and clock state of the nuclear clock are also presented. The nuclear spin quantum numbers are $I_g = 5/2$ for the ground state and $I_m = 3/2$ for the isomer state.

transition, and present the transition wavelengths, radiative times and hyperfine structure constants in Fig. 1. Details of the calculations are provided in the Supplementary Materials (SM).

Clock Performance. To comprehensively assess the performance of the nuclear clock based on $^{229}Th^{6+}$, it is essential to evaluate the effects of various external fields. Our evaluation of the nuclear clock is based on the average of two transitions,

$$\begin{aligned}
\nu_1 &= \nu(|^3P_2, I_g, 9/2, +9/2\rangle \leftrightarrow |^3P_2, I_m, 7/2, +7/2\rangle),\\
\nu_2 &= \nu(|^3P_2, I_g, 9/2, -9/2\rangle \leftrightarrow |^3P_2, I_m, 7/2, -7/2\rangle),\\
\nu_{\text{clock}} &= \frac{\nu_1 + \nu_2}{2},
\end{aligned} \tag{1}$$

where the last two quantum numbers denote the total angular momentum F and its projection M. The invariance of the electronic state in this transition can be explicitly seen by expressing the coupled state $|F, M\rangle$ in terms of the uncoupled basis $|I, M_I\rangle|J, M_J\rangle$:

$$\begin{aligned}
|^3P_2, I_g, 9/2, \pm 9/2\rangle &= |I_g, \pm I_g\rangle|2, \pm 2\rangle,\\
|^3P_2, I_m, 7/2, \pm 7/2\rangle &= |I_m, \pm I_m\rangle|2, \pm 2\rangle.
\end{aligned} \tag{2}$$

Owing to this invariance, the linear Zeeman shift, the electric quadrupole shift, and the blackbody radiation (BBR) shift at 300 K in this nuclear clock transition arise solely from the nucleus together with the shielding effect of the surrounding electrons. Among them, the linear Zeeman shift is canceled by averaging the two transitions. After accounting for electronic shielding, the nuclear electric quadrupole contribution in an electric field gradient of 1 kV/cm^2 is suppressed to a fractional level below 10^{-19}.[11,28] Furthermore, the differential nuclear scalar electric dipole ($E1$) polarizability is estimated to be $\Delta\alpha_0 < 10^{-16} e a_0^3$, which leads to a BBR-induced fractional shift at 300 K below 10^{-20}.[29]

Due to the absence of visible-laser-driven electric dipole transitions, sympathetic cooling becomes necessary. Lased-cooled $^{40}Ca^+$ ions are a promising choice for the sympathetic cooling of $^{229}Th^{6+}$, as they have a comparable charge-to-mass ratio to $^{229}Th^{6+}$ and can also serve as logic ions for the $^{229}Th^{6+}$ ionic clock. Assuming the $^{229}Th^{6+}$ can reach a temperature of 1 mK (typical temperature of $^{40}Ca^+$ after Doppler cooling), the fractional second-order Doppler shift is estimated to be -6.0×10^{-19}. Utilizing sideband cooling[30] or electrically induced transparency cooling[31] on $^{40}Ca^+$ is expected to reduce this shift to below 10^{-19}. Moreover, the fractional scalar Stark shift induced from micro-motion is also suppressed to below 1×10^{-20} due to the small differential $E1$ scalar polarizability of nucleus.[29]

However, because the quadratic Zeeman shift arises primarily from second-order mixing among hyperfine levels, the invariance of the electronic state alone does not guarantee that the quadratic Zeeman shift is purely nuclear. More precisely, for a hyperfine level $|I, J, F, M\rangle$ the dc quadratic Zeeman shift is generated by the magnetic interaction with other hyperfine states $|I, J, F', M\rangle$ with $F' \neq F$ but the same magnetic quantum number M. In the nuclear transitions considered here both levels are stretched states with $F_{\max} = I + J$ and $M = \pm F_{\max}$. For $M = \pm F_{\max}$ there are no other hyperfine states $|I, J, F', M\rangle$ (since any $F' < F_{\max}$ necessarily satisfies $F' < M$), and therefore the usual second-order hyperfine mixing that produces an electronic contribution to the quadratic Zeeman shift is forbidden. As a result, the dc quadratic Zeeman shift for the nuclear clock transition is overwhelmingly dominated by the nuclear contribution and is expected to be below 10^{-20}.[11,21]

The ac Zeeman shift induced by the radio frequency field in the ion trap is of particular interest.[12] This magnetic field can be decomposed into a component parallel to the quantization axis, $B_\parallel$, and a perpendicular component, $B_\perp$. For the state $|F, M\rangle$, the ac Zeeman shift is given by

$$\begin{aligned}
&\delta\nu_{\text{ac,M2}}\\
&= \frac{(\mu_B g_J B_\parallel)^2}{4h} \sum_{F'M'} \sum_{\sigma} \frac{|\langle FM|J_z|F'M'\rangle|^2}{\Delta E_{FM,F'M'} + \sigma h\Omega}\\
&\quad + \frac{(\mu_B g_J B_\perp)^2}{16h} \sum_{F'M'} \sum_{\sigma} \frac{|\langle FM|J_+|F'M'\rangle|^2}{\Delta E_{FM,F'M'} + \sigma h\Omega}\\
&\quad + \frac{(\mu_B g_J B_\perp)^2}{16h} \sum_{F'M'} \sum_{\sigma} \frac{|\langle FM|J_-|F'M'\rangle|^2}{\Delta E_{FM,F'M'} + \sigma h\Omega},
\end{aligned} \tag{3}$$

where h is the Planck's constant, μ_B is the Bohr magneton, $\Delta E_{FM,F'M'}$ denotes the energy gap $E_{FM} - E_{F'M'}$, Ω represents the trap drive frequency, and the summation of σ is performed over $\{+1, -1\}$. The wavefunctions and energies are obtained by non-perturbatively diagonalizing the hyperfine interaction Hamiltonian H_{hfi} combined with the external dc magnetic field term $g_J\mu_B B_0 J_z$. Further details can be found in the SM.

Figure 2 presents representative ac Zeeman curves as functions of the dc magnetic field B_0 at several trap drive frequencies Ω. The zero crossings of these curves define the

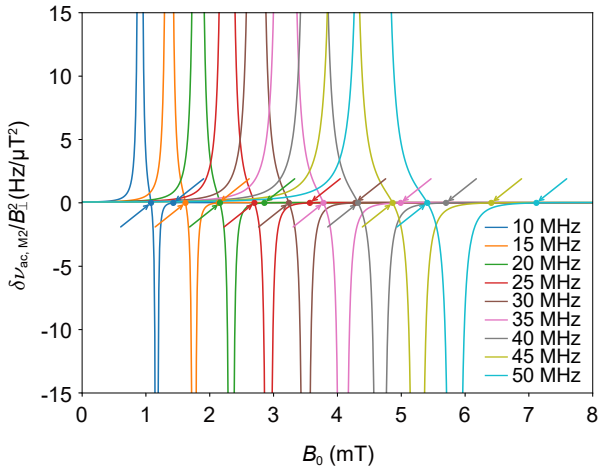

Fig. 2. Representative ac Zeeman shifts versus the dc magnetic field B_0 for several trap drive frequencies Ω. Each curve exhibits two zero crossings, corresponding to the first and second magic dc magnetic fields (1st magic B_0 and 2nd magic B_0). Arrows indicate the positions of these zero crossings on each curve.

"magic" dc magnetic fields at which the ac Zeeman shift vanishes; the dependence of these magic-field values on Ω is plotted in Fig. 3(a). We extract the two zero crossings for each Ω (denoted below as the 1st and 2nd magic B_0) and use them to evaluate the sensitivity of the residual ac Zeeman uncertainty to dc field fluctuations, as shown in Fig. 3(b).

Similar to the $^{229}Th^{3+}$ case,[12] the magic dc magnetic fields for $^{229}Th^{6+}$ depend approximately linearly on the trap drive frequency Ω, as shown in Fig. 3(a). The 1st magic B_0 is always smaller than the 2nd magic B_0, but, as visible in Fig. 2, the slope of the ac Zeeman curve at the 1st magic B_0 is significantly larger than that at the 2nd magic B_0. Consequently, for a given dc field fluctuation ΔB_0, the induced uncertainty of the ac Zeeman shift is larger at the 1st magic B_0 than that at the 2nd. We quantify this effect in Fig. 3(b) by plotting the fractional uncertainty of the ac Zeeman shift for $\Delta B_0 = 1\,\mu\text{T}$ with $B_\perp$ fixed at $1\,\mu\text{T}$. For the parameter range studied, a dc-field fluctuation of $\Delta B_0 = 1\,\mu\text{T}$ yields fractional uncertainties below 1×10^{-19} when $\Omega \geq 25\,\text{MHz}$.

Precise determination of the magic dc magnetic field, B_0, can be achieved by scanning in the vicinity of the magic B_0 region, as illustrated in Fig. 3(a). This can be complemented by the technique for measuring $B_\perp$ via laser-cooling $^{40}Ca^+$ ion.[32] Alternatively, one may directly compute the magic B_0 by accurately measuring the hyperfine structure constants and the Landé g-factor of the ground electronic state.

Nuclear Information Extraction. By utilizing the ionic clock transition $|^3P_2\rangle \leftrightarrow |^3P_0\rangle$, one can determine the hyperfine structure constants and the charge radius difference between the nuclear ground state and the isomer state. This information is also valuable for assessing the alpha-sensitivity of the nuclear clock.[15]

Specifically, when the nucleus is in its nuclear ground state, the clock transition frequency ν_0^{g} (without considering hyperfine splitting), along with the hyperfine structure constants A_{g} and B_{g}, can be determined by measuring the following three clock transitions (M_I is arbitrary):

$$\begin{aligned}
\nu_1^{\text{g}} &\equiv \nu(|^3P_2, I_{\text{g}}, 9/2, \pm 9/2\rangle \rightarrow |^3P_0, I_{\text{g}}, \pm M_I\rangle),\\
\nu_2^{\text{g}} &\equiv \nu(|^3P_2, I_{\text{g}}, 7/2, \pm 7/2\rangle \rightarrow |^3P_0, I_{\text{g}}, \pm M_I\rangle),\\
\nu_3^{\text{g}} &\equiv \nu(|^3P_2, I_{\text{g}}, 3/2, \pm 1/2\rangle \rightarrow |^3P_0, I_{\text{g}}, \pm M_I\rangle).
\end{aligned}$$

For the nuclear isomer state, the clock transition frequency ν_0^{m} (without considering hyperfine splitting) and the hyperfine structure constants A_{m} and B_{m} also can be determined by measuring the following three clock transitions:

$$\begin{aligned}
\nu_1^{\text{m}} &\equiv \nu(|^3P_2, I_{\text{m}}, 7/2, \pm 7/2\rangle \rightarrow |^3P_0, I_{\text{m}}, \pm M_I\rangle),\\
\nu_2^{\text{m}} &\equiv \nu(|^3P_2, I_{\text{m}}, 3/2, \pm 1/2\rangle \rightarrow |^3P_0, I_{\text{m}}, \pm M_I\rangle),\\
\nu_3^{\text{m}} &\equiv \nu(|^3P_2, I_{\text{m}}, 1/2, \pm 1/2\rangle \rightarrow |^3P_0, I_{\text{m}}, \pm M_I\rangle).
\end{aligned}$$

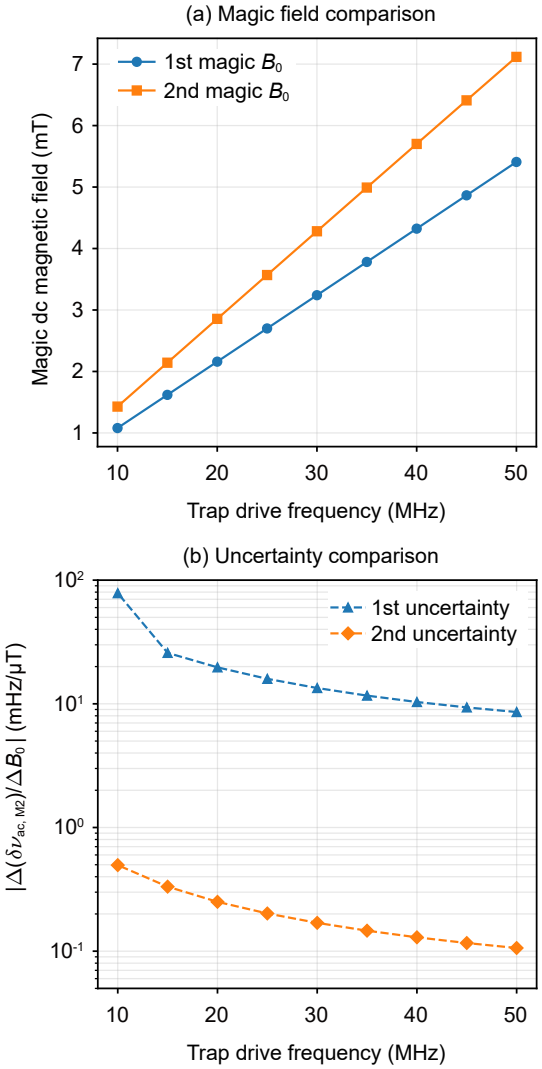

Fig. 3. (a) First and second magic dc magnetic fields (1st and 2nd magic B_0) as functions of the trap drive frequency Ω. (b) Fractional uncertainty of the ac Zeeman shift resulting from a dc field fluctuation $\Delta B_0 = 1\,\mu\text{T}$, with $B_\perp$ fixed at $1\,\mu\text{T}$.

Table 1. The Zeeman shifts $\delta\nu_{\rm M2}$ and electric quadruple shifts $\delta\nu_{\rm EQ}$ for six clock transitions, with the values given in units of Hz. Quantum numbers F and M for ground states are labeled. The calculation assumes a magnetic field $B_0 = 5\,\mu$T, a perpendicular magnetic field component $B_\perp = 1\,\mu$T, a trap drive frequency $\Omega = 25\,$MHz, and an electric field gradient $\frac{\partial \mathcal{E}_z}{\partial z} = 1\,$kV/cm.

Nuclear spin	F, M	$\delta\nu_{\rm dc,M2}$	$\delta\nu_{\rm ac,M2}$	$\delta\nu_{\rm EQ}$
$I_{\rm g}$	$9/2, \pm 9/2$		-0.0128	0.2724
	$7/2, \pm 7/2$	0.2834	-0.4549	0.0454
	$3/2, \pm 1/2$	0.1883	-0.0453	0.1362
$I_{\rm m}$	$7/2, \pm 7/2$		-0.0805	0.2724
	$3/2, \pm 1/2$	0.1914	-0.0137	
	$1/2, \pm 1/2$	-1.6609	-0.0332	

Due to the lack of hyperfine structure and electric quadruple moment in the clock state, the Zeeman shifts and electric quadruple shifts arise almost entirely from the ground state. We have selected clock states with relatively small external field shifts, as shown in Table 1. When the dc magnetic field uncertainty $\Delta B_0 = 1\,\mu$T, the resulting uncertainties in these external field shifts are well-controlled. The single-ion fractional instability can be estimated by $\sigma_y(t) = \frac{0.412}{\nu_{\rm clock}\sqrt{\tau t}}$,[1] where $\nu_{\rm clock}$ is the ionic clock transition frequency and τ is the radiative lifetime of the ionic clock state, give rise to $\sigma_y(t) = 7 \times 10^{-16}/\sqrt{t/\rm s}$. Hence, achieving sub-Hz instability in the measurement only requires a few seconds of averaging.

The calculated differential static $E1$ scalar polarizability is $0.11ea_0^3$, resulting in a BBR shift of $-0.93\,$mHz (fractional shift -2.0×10^{-18}) in 300 K. Motion-induced shifts are estimated to be the same as those in the nuclear clock transition. Since these shifts do not depend on the quantum number F, they are incorporated into ν_0. Consequently, the values of A and B obtained by solving the linear equations achieve Hz-level precision.

Variations in the nuclear charge radius $\Delta\langle r^2\rangle_{229} = \langle r^2\rangle_{229\rm m} - \langle r^2\rangle_{229\rm g}$, give rise to a field shift $\Delta\nu_{\rm FS} = F_{\rm FS}\Delta\langle r^2\rangle_{229} = \nu_0^{\rm m} - \nu_0^{\rm g}$. The field shift factor is calculated as $F_{\rm FS} = -0.192(18)\,{\rm GHz/fm^2}$, and its uncertainty estimation can be found in the SM. At the Hz-level precision, the uncertainty in $\Delta\langle r^2\rangle_{229}$ can be reduced to 9%, which dominated by the uncertainty of theoretical calculations. Improved theoretical calculations (e.g., via the all-order method in the pCI package[33]) can further decrease this uncertainty. Moreover, the ratio $A_{\rm m}/A_{\rm g}$ enables determination of the nuclear magnetic moment ratio with a precision of 10^{-9}, significantly surpassing the current result, $\mu_{\rm m}/\mu_{\rm g} = -1.04(15)$.[13]

The existence of a metastable state with $J = 0$ also opens up the possibility of establishing the nuclear clock transition $|^3P_0, I_{\rm g}\rangle \leftrightarrow |^3P_0, I_{\rm m}\rangle$. In this nuclear clock, both the dc Zeeman shift and electric quadrupole shift still vanish inherently. Additionally, because of the absence of hyperfine structure, the ac Zeeman shift becomes negligible even without applying a magic dc magnetic field. However, this approach comes at a cost: the interrogation time is limited by the lifetime of the metastable state $|^3P_0\rangle$.

Optical Repumping. A closed cycle of clock operation involves the optical repumping process from the clock state back to the ground state. In Th^{6+}, there exist two excited electronic states $|^3P_1, I_{\rm g}\rangle$ and $|^1D_2, I_{\rm g}\rangle$ near and slightly above the nuclear clock state, each with a lifetime of approximately 0.1 ms. Population in the nuclear clock state can be transferred to these electronic levels with infrared light; the excited electronic states then decay spontaneously back to the electronic ground manifold, completing the repumping step.

However, a direct transition that simultaneously changes both the nuclear state and the electronic configuration is forbidden in the absence of coupling between nuclear and electronic degrees of freedom. Electromagnetic operators that drive electronic excitations do not connect different nuclear spin manifolds, so the transition matrix element vanishes. Hyperfine interactions couple nuclear and electronic degrees of freedom and induce small admixtures of states with different I and J. As a result, an eigenstate whose nuclear part is predominantly the nuclear isomer state $I_{\rm m}$ acquires a small admixture of the nuclear ground state component $I_{\rm g}$, and vice versa. Ordinary electronic transition operators therefore obtain a nonzero, though suppressed, transition matrix element between the mixed states; this weakly allowed channel is the EB transition exploited for optical repumping.[34] The theory of nuclear hyperfine mixing has been derived in references.[24,35] Below we directly present the state-mixing results for Th^{6+}, where underline denotes the mixed eigenstates in the presence of hyperfine interactions,

$$\begin{aligned}\underline{|^3P_2, I_{\rm m}, F\rangle} &= |^3P_2, I_{\rm m}, F\rangle + b(F)\langle I_{\rm m}||\mu||I_{\rm g}\rangle \\ &\quad\times|^3P_1, I_{\rm g}, F\rangle, \qquad (4)\\ \underline{|^3P_1, I_{\rm g}, F'\rangle} &= |^3P_1, I_{\rm g}, F'\rangle - b(F')\langle I_{\rm m}||\mu||I_{\rm g}\rangle \\ &\quad\times|^3P_2, I_{\rm m}, F'\rangle, \qquad (5)\end{aligned}$$

where

$$\begin{aligned}b(F) &= (-1)^{I_{\rm m}+1+F}\begin{Bmatrix} I_{\rm g} & 1 & F \\ 2 & I_{\rm m} & 1\end{Bmatrix} \\ &\quad\times\frac{\langle^3P_1||T_1||^3P_2\rangle}{E(^3P_2) - E(^3P_1) + \omega_{\rm N}}, \qquad (6)\end{aligned}$$

where $\omega_{\rm N}$ is nuclear transition frequency, μ is $M1$ transition operator, and T_1 is electronic operator. The reduced matrix element $\langle^3P_1||T_1||^3P_2\rangle$ is calculated as 0.863 a.u., resulting a maximal mixing coefficient $b(7/2) \approx -13$ a.u. The reduced matrix element $\langle I_{\rm m}||\mu||I_{\rm g}\rangle$ is fixed as 1.59×10^{-6} a.u. based on the radiative lifetime measurements.[8] We only consider the nuclear hyperfine mixing between $|^3P_2, I_{\rm m}\rangle$ and $|^3P_1, I_{\rm g}\rangle$ states because the other states have smaller reduced matrix elements of T_1 operator and larger energy level differences to those states.

We denote $|^3P_2, I_{\rm m}\rangle$, $|^3P_1, I_{\rm g}\rangle$ and $|^1D_2, I_{\rm g}\rangle$ as $|1\rangle$, $|2\rangle$, and $|3\rangle$, respectively, as shown in Fig. 1. The matrix ele-

ment of EB $M1$ transition can be calculated as:

$$\langle 1,F||\mu||2,F'\rangle = b(F)\langle I_{\rm m}||\mu||I_g\rangle\langle 2,F||\mu||2,F'\rangle - b(F')\langle I_{\rm m}||\mu||I_g\rangle\langle 1,F||\mu||1,F'\rangle, \quad (7)$$

$$\langle 1,F||\mu||3,F'\rangle = b(F)\langle I_{\rm m}||\mu||I_{\rm g}\rangle\langle 2,F||\mu||3,F'\rangle. \quad (8)$$

We introduce the enhancement factor $\beta(F,F')$, as the ratio of the EB transition line strength to that of the nuclear clock transition,

$$\beta_{1\leftrightarrow 2}(F,F') \equiv \Big[b(F)\langle 2,F||\mu||2,F'\rangle - b(F')\langle 1,F||\mu||1,F'\rangle\Big]^2, \quad (9)$$

$$\beta_{1\leftrightarrow 3}(F,F') \equiv \Big[b(F)\langle 2,F||\mu||3,F'\rangle\Big]^2. \quad (10)$$

Hence, the decay rate of EB transition $\gamma_{\rm EB}$ can be written as

$$\gamma_{\rm EB} = \left(\frac{\omega}{\omega_{\rm N}}\right)^3 \beta(F,F')\gamma_{\rm N}\frac{2I_{\rm m}+1}{2F'+1}, \quad (11)$$

where ω is transition frequency, $\omega_{1\leftrightarrow 2} = E(^3P_1) - E(^3P_2) - \omega_{\rm N}$ and $\omega_{1\leftrightarrow 3} = E(^1D_2) - E(^3P_2) - \omega_{\rm N}$. $\gamma_{\rm N} = 3.91\times 10^{-4}\,{\rm s}^{-1}$ is the decay rate of nuclear isomer state of bare nucleus in vacuum, which calculated from radiative lifetime $\tau = 641\,{\rm s}$ in crystal and refractive index $n = 1.586$.[6,8,36] The decay rate of EB transition $\gamma_{\rm EB}$ is suppressed by the factor $(\omega/\omega_{\rm N})^3$, and thus has a negligible effect on the branching ratios of the spontaneous decay from the intermediate states $|2\rangle$ and $|3\rangle$.

For the EB transition $|1\rangle \leftrightarrow |2\rangle$, the maximum enhancement factor, $\beta \approx 0.449$, is achieved when $F' = 7/2$. For the EB transition $|1\rangle \leftrightarrow |3\rangle$, the maximum enhancement factor, $\beta \approx 0.003$, is achieved when $F' = 9/2$. In both cases, we set $F = 7/2$ as the fixed quantum number. An enhancement factor $\beta < 1$ implies that higher laser power is required, compared to nuclear clock excitation. However, given the maturity of high-power infrared laser technology, it is feasible to achieve rapid nuclear deexcitation via the EB transition in the infrared region.

We investigate the state-transfer dynamics by solving the following quantum master equation (in units of $\hbar = 1$):[37]

$$\dot{\rho} = -{\rm i}\,[H_{\rm I},\rho] + \mathcal{L}\rho, \quad (12)$$

where ρ is the density matrix, $H_{\rm I}$ is the interaction Hamiltonian, and $\mathcal{L}$ is the Lindblad operator. In our system, we relabel the hyperfine states $|^3P_2, I_{\rm m}, F = 7/2\rangle$, $|^3P_1, I_{\rm g}, F = 7/2\rangle$, $|^1D_2, I_{\rm g}, F = 9/2\rangle$ as $|1\rangle$ to $|3\rangle$, respectively, states $|^3P_0, I_{\rm g}\rangle$, $|^3P_2, I_{\rm g}\rangle$ are labeled as $|4\rangle$ and $|5\rangle$, respectively, as shown in Fig. 4. The initial state is the nuclear clock state $|1\rangle$, which is excited to the intermediate states $|2\rangle$ or $|3\rangle$ via the EB transition. These intermediate states then decay spontaneously as $|2\rangle$ to $|4\rangle$ and $|5\rangle$, $|3\rangle$ to $|5\rangle$, respectively. The probabilities of all other decay channels are sufficiently low to be negligible.

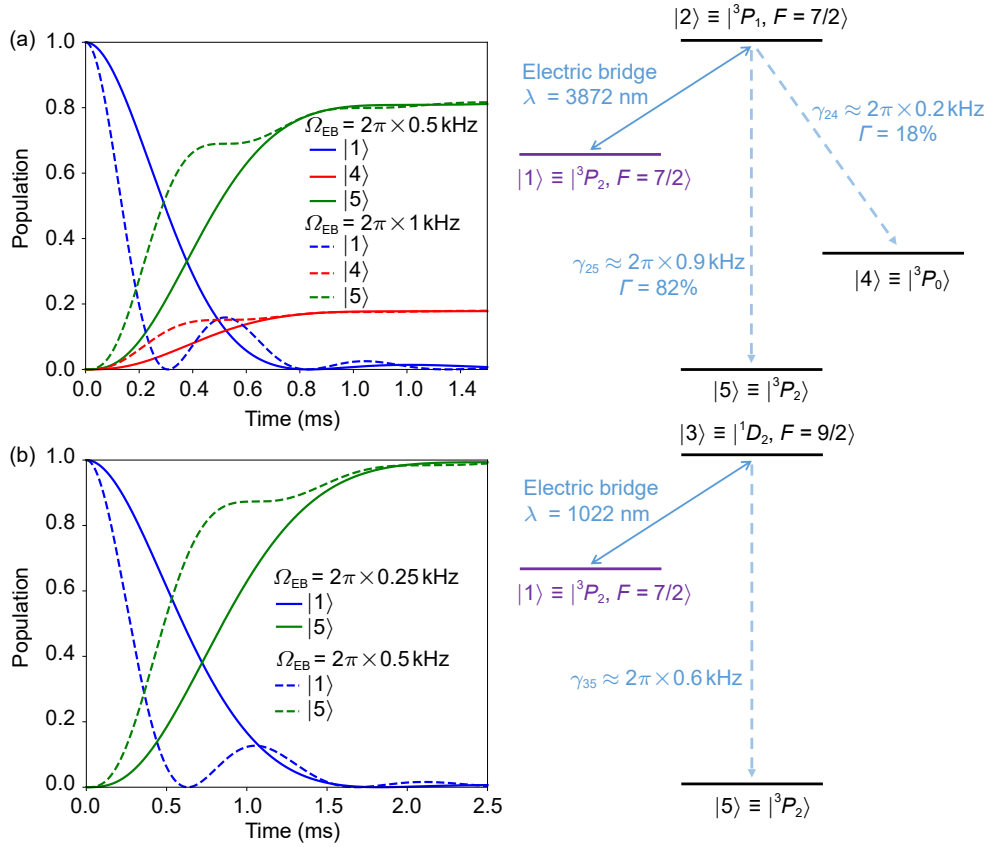

Fig. 4. Population dynamics of the low-lying states with state (a) $|2\rangle$ and (b) $|3\rangle$ serving as the intermediate state. The schematic diagrams on the right illustrate the Rabi frequencies $\Omega_{\rm EB}$, decay rates γ, and branching ratios Γ. The purple energy levels are the nuclear isomer states.

The interaction Hamiltonian $H_{\rm I}$ is given by

$$H_{\rm I} = \Omega_{{\rm EB},1\leftrightarrow i}(|1\rangle\langle i| + |i\rangle\langle 1|), \tag{13}$$

where i represents intermediate states $|2\rangle$ or $|3\rangle$ and the Rabi frequency $\Omega_{\rm EB}$ can be calculated by

$$\Omega_{\rm EB} = \frac{1}{\hbar}\sqrt{\frac{2I_\ell}{c^3\epsilon_0}}\sqrt{\beta}\langle I_{\rm m}||\mu||I_{\rm g}\rangle, \tag{14}$$

where I_ℓ represents the laser intensity. In our calculation, a laser intensity of $I_\ell = 1.8\times10^6\,{\rm W/m^2}$ is considered in the case of $|2\rangle$ as the intermediate state (corresponding to a laser power of approximately 7 mW and a beam spot radius of 50 μm). This configuration yields a Rabi frequency of $\Omega_{{\rm EB},1\leftrightarrow2} = 2\pi\times0.5\,{\rm kHz}$. In the case of $|3\rangle$ as the intermediate state, we fix the laser intensity $I_\ell = 6.1\times10^7\,{\rm W/m^2}$ (corresponding to a laser power of approximately 240 mW and a beam spot radius of 50 μm). This configuration yields a Rabi frequency of $\Omega_{{\rm EB},1\leftrightarrow3} = 2\pi\times0.25\,{\rm kHz}$.

Based on our estimation of the Rabi frequencies for the EB transitions, we investigated the population dynamics for different intermediate states, as shown in Fig. 4. The results indicate that both channels can achieve optical repumping on the millisecond timescale. Although the intermediate state $|2\rangle$ allows for slightly faster repumping and has a lower requirement for laser power, its multiple spontaneous decay channels result in a 18% probability of decaying into the long-lived state $|4\rangle$. In contrast, the spontaneous decay channels $|3\rangle\rightarrow|2\rangle$ and $|3\rangle\rightarrow|4\rangle$ can be effectively neglected, resulting in a probability greater than 98% of decaying into the ground state $|5\rangle$. Moreover, the required laser operates at a wavelength of 1022 nm, which is a mature and readily available technology. This further underscores the practicality of our approach.

We also investigate the influence of Rabi frequency increase on population dynamics, as shown in the dotted line of Fig. 4. When the Rabi frequency is increased, the time required for optical repumping is decreased significantly. Additionally, the repumping time is limited by the spontaneous decay rates of the intermediate state, this behavior can be understood in the limiting case when $\Omega \gg \gamma$, where the ground-state population evolves approximately as

$$n_5(t) \approx \Gamma - \exp\left(-\frac{\gamma t}{2}\right), \tag{15}$$

where Γ is branching ratio. Conversely, in the limit $\Omega \ll \gamma$, the ground-state population follows

$$n_5(t) \approx \Gamma - \exp\left(-\frac{\Omega^2 t}{\gamma}\right), \tag{16}$$

corresponding to a characteristic optical repumping time of $T = \gamma/\Omega^2$. Therefore, when the intermediate state exhibits $E1$ spontaneous decays ($\gamma\sim$ MHz), this limit is easily reached, resulting in a characteristic repumping time that may exceed the lifetime of the nuclear isomer state. Consequently, the optimal condition for efficient optical repumping is $\Omega \approx \gamma$. In highly charged ions, this condition is readily satisfied: many intermediate states decay predominantly via $M1$ transitions, with decay rates on the order of kHz, while strong nucleus–electron coupling further enhances the Rabi frequency.

Current 148 nm laser sources can achieve the Rabi frequency of approximately 0.4 Hz for the ^{229}Th nuclear clock transition.[6] This corresponds to a π-pulse duration on the order of seconds, which is substantially longer than the millisecond-scale repumping time. The repumping process produces ultraviolet fluorescence and induces changes in the electronic state. Thus, this enables state readout through either ultraviolet fluorescence detection or quantum logic spectroscopy. Consequently, the total duration of a closed clock cycle remains on the order of seconds.

In contrast, for Th^{3+} ion, the nuclear clock state $|5f_{5/2}, I_{\rm m}\rangle$ mixes with $|7p_{3/2}, I_{\rm g}\rangle$, giving rise to a repumping pathway,

$$|5f_{5/2}, I_{\rm m}\rangle \;\rightarrow\; |6d_{3/2}, I_{\rm g}\rangle \;\rightarrow\; |5f_{5/2}, I_{\rm g}\rangle.$$

However, the EB transition $|5f_{5/2}, I_{\rm m}\rangle \;\rightarrow\; |6d_{3/2}, I_{\rm g}\rangle$ occurs in the ultraviolet region (172 nm) and exhibits a small enhance factor on the order of 0.001.[38] This makes it challenging to achieve the optimal condition $\Omega \approx \gamma \approx 2\pi\times0.2\,{\rm MHz}$.[39]

For ^{229}Th-doped crystals, laser/photo-induced quenching has been experimentally verified, but the mechanism of quenching remains unclear.[40,41] A possible mechanism is similar to that in $^{229}Th^{6+}$: nuclear clock states are excited via the EB transition to higher defect states and then undergo spontaneous decay back to the ground state.[42,43] Therefore, searching for defect states that satisfy the optimal condition $\Omega \approx \gamma$ might be helpful for rapid laser/photo-induced quenching in solid-state nuclear clock.

In conclusion, our study demonstrates that the electronic clock transition in $^{229}Th^{6+}$ ions serves as an effective probe for information on nuclear structure. By averaging over tens of seconds, the isomer shift can be measured to sub-Hz precision. When combined with theoretical calculations, this reduces the uncertainty in nuclear charge radius variations to 9% or lower, thereby enabling a more accurate determination of the sensitivity factor of the nuclear transition frequency to variations in the fine-structure constant. Moreover, the favorable electronic structure and radiative transition properties of Th^{6+} render it a promising platform for nuclear clocks, enabling efficient optical repumping and presenting promising potential for advanced precision measurements.

Acknowledgements. This work was supported by the Strategic Priority Research Program of the Chinese Academy of Sciences (Grant No. XDB0920000), the National Key Research and Development Program of China (Grant No. 2022YFB3904002), and the National Natural Science Foundation of China (Grant No. 12341401).

References

[1] Kozlov M, Safronova M, Crespo López-Urrutia J, and Schmidt P 2018 *Rev. Mod. Phys.* **90** 045005

[2] Ludlow A D, Boyd M M, Ye J, Peik E, and Schmidt P 2015 *Rev. Mod. Phys.* **87** 637
[3] Tkalya E, Varlamov V, Lomonosov V, and Nikulin S 1996 *Phys. Scr.* **53** 296
[4] Peik E and Tamm C 2003 *Europhys. Lett.* **61** 181
[5] Thirolf P G, Kraemer S, Moritz D, and Scharl K 2024 *Eur. Phys. J. Spec. Top.* **233** 1113
[6] Zhang C, Ooi T, Higgins J S *et al.* 2024 *Nature* **3** 63
[7] Zhang C, von der Wense L, Doyle J F *et al.* 2024 *Nature* **636** 603
[8] Tiedau J, Okhapkin M, Zhang K *et al.* 2024 *Phys. Rev. Lett.* **132** 182501
[9] Elwell R, Schneider C, Jeet J, Terhune J, Morgan H, Alexandrova A, Tran Tan H, Derevianko A, and Hudson E R 2024 *Phys. Rev. Lett.* **133** 013201
[10] Fuchs E, Kirk F, Madge E, Paranjape C, Peik E, Perez G, Ratzinger W, and Tiedau J 2025 *Phys. Rev. X* **15** 021055
[11] Campbell C J, Radnaev A G, Kuzmich A, Dzuba V A, Flambaum V V, and Derevianko A 2012 *Phys. Rev. Lett.* **108** 120802
[12] Beloy K 2023 *Phys. Rev. Lett.* **130** 103201
[13] Thielking J, Okhapkin M V, G lowacki P, Meier D M, Von Der Wense L, Seiferle B, Düllmann C E, Thirolf P G, and Peik E 2018 *Nature* **556** 321
[14] Kälber W, Rink J, Bekk K, Faubel W, Göring S, Meisel G, Rebel H, and Thompson R C 1989 *Z. Physik A - Atomic Nuclei* **334** 103
[15] Beeks K, Kazakov G A, Schaden F *et al.* 2024 arXiv:2407.17300 [nucl-th]
[16] Safronova M, Porsev S, Kozlov M, Thielking J, Okhapkin M, G lowacki P, Meier D, and Peik E 2018 *Phys. Rev. Lett.* **121** 213001
[17] Porsev S, Safronova M, and Kozlov M 2021 *Phys. Rev. Lett.* **127** 253001
[18] Dzuba V A and Flambaum V V 2025 *Phys. Rev. A* **111** L041103
[19] Dzuba V A and Flambaum V V 2025 *Phys. Rev. A* **111** 053109
[20] Yudin V I, Taichenachev A V, Prudnikov O N, Basalaev M Y, Goncharov A N, Chepurov S V, and Pal'chikov V G 2025 *Jetp Lett.* **121** 345
[21] Flambaum V V, Dzuba V A, and Peik E 2025 *Phys. Rev. A* **112** 023103
[22] Bilous P V, Bekker H, Berengut J C, Seiferle B, von der Wense L, Thirolf P G, Pfeifer T, López-Urrutia J R C, and Pálffy A 2020 *Phys. Rev. Lett.* **124** 192502
[23] Porsev S G, Cheung C, and Safronova M S 2021 *Quantum Sci. Technol.* **6** 034014
[24] Shabaev V, Glazov D, Ryzhkov A, Brandau C, Plunien G, Quint W, Volchkova A, and Zinenko D 2022 *Phys. Rev. Lett.* **128** 043001
[25] Beloy K, Dzuba V, and Brewer S 2020 *Phys. Rev. Lett.* **125** 173002
[26] Rodrigues G, Indelicato P, Santos J, Patté P, and Parente F 2004 *Atom. Data Nucl. Data* **86** 117
[27] Kahl E and Berengut J 2019 *Comput. Phys. Commun.* **238** 232
[28] Litvinova E, Feldmeier H, Dobaczewski J, and Flambaum V 2009 *Phys. Rev. C* **79** 064303
[29] von Neumann-Cosel P and Tamii A 2025 *Front. Phys.* **13** 1629987
[30] Cui K f, Shang J j, Chao S j, Wang S m, Yuan J b, Zhang P, Cao J, Shu H l, and Huang X r 2018 *J. Phys. B: At. Mol. Opt. Phys.* **51** 045502
[31] Huang C, Wang C, Zhang H, Hu H, Wang Z, Mao Z, Li S, Hou P, Wu Y, Zhou Z, and Duan L 2024 *Phys. Rev. Lett.* **133** 113204
[32] Ma Z, Zhang B, Huang Y, Hu R, Zeng M, Gao K, and Guan H 2024 *Phys. Rev. A* **110** 063102
[33] Cheung C, Kozlov M G, Porsev S G, Safronova M S, Tupitsyn I I, and Bondarev A I 2025 *Comput. Phys. Commun.* **308** 109463
[34] Porsev S G and Flambaum V V 2010 *Phys. Rev. A* **81** 032504
[35] Wang W, Zou F, Fritzsche S, and Li Y 2024 *Phys. Rev. Lett.* **133** 223001
[36] Tkalya E V 2000 *Jetp Lett.* **71** 311
[37] Johansson J, Nation P, and Nori F 2012 *Comput. Phys. Commun.* **183** 1760
[38] Porsev S G and Flambaum V V 2010 *Phys. Rev. A* **81** 032504
[39] Li F C, Qiao H X, Tang Y B, and Shi T Y 2022 *J. Quant. Spectrosc. Radiat. Transfer* **288** 108241
[40] Schaden F, Riebner T, Morawetz I, De Col L T, Kazakov G A, Beeks K, Sikorsky T, Schumm T, Zhang K, Lal V, Zitzer G, Tiedau J, Okhapkin M V, and Peik E 2025 *Phys. Rev. Research* **7** L022036
[41] Terhune J E S, Elwell R, Tan H B T, Perera U C, Morgan H W T, Alexandrova A N, Derevianko A, and Hudson E R 2025 *Phys. Rev. Research* **7** L022062
[42] Nickerson B S, Pimon M, Bilous P V, Gugler J, Kazakov G A, Sikorsky T, Beeks K, Grüneis A, Schumm T, and Pálffy A 2021 *Phys. Rev. A* **103** 053120
[43] Nickerson B S, Pimon M, Bilous P V, Gugler J, Beeks K, Sikorsky T, Mohn P, Schumm T, and Pálffy A 2020 *Phys. Rev. Lett.* **125** 032501